Photoionization of Co+ and electron-impact excitation of Co2 + using the Dirac R-matrix method

Monthly Notices
of the
ROYAL ASTRONOMICAL SOCIETY

MNRAS **462,** 3350–3360 (2016)
Advance Access publication 2016 July 28

doi:10.1093/mnras/stw1843

Photoionization of Co^+ and electron-impact excitation of Co^{2+} using the Dirac *R*-matrix method

N. B. Tyndall,* C. A. Ramsbottom,* C. P. Ballance and A. Hibbert
School of Mathematics and Physics, The Queen's University of Belfast, Belfast BT7 1NN, UK

Accepted 2016 July 25. Received 2016 July 25; in original form 2016 April 29

ABSTRACT

Modelling of massive stars and supernovae (SNe) plays a crucial role in understanding galaxies. From this modelling we can derive fundamental constraints on stellar evolution, mass-loss processes, mixing, and the products of nucleosynthesis. Proper account must be taken of all important processes that populate and depopulate the levels (collisional excitation, de-excitation, ionization, recombination, photoionization, bound–bound processes). For the analysis of Type Ia SNe and core collapse SNe (Types Ib, Ic and II) Fe group elements are particularly important. Unfortunately little data is currently available and most noticeably absent are the photoionization cross-sections for the Fe-peaks which have high abundances in SNe. Important interactions for both photoionization and electron-impact excitation are calculated using the relativistic Dirac atomic *R*-matrix codes (DARC) for low-ionization stages of Cobalt. All results are calculated up to photon energies of 45 eV and electron energies up to 20 eV. The wavefunction representation of Co III has been generated using GRASP0 by including the dominant $3d^7$, $3d^6[4s, 4p]$, $3p^43d^9$ and $3p^63d^9$ configurations, resulting in 292 fine structure levels. Electron-impact collision strengths and Maxwellian averaged effective collision strengths across a wide range of astrophysically relevant temperatures are computed for Co III. In addition, statistically weighted level-resolved ground and metastable photoionization cross-sections are presented for Co II and compared directly with existing work.

Key words: atomic data – atomic processes – scattering – supernovae: general – infrared: general.

1 INTRODUCTION

Lowly ionized species of Cobalt are often observed in astrophysical objects such as supernovae (SNe), cool stars (Bergemann, Pickering & Gehren 2010), early-type stars (Smith & Dworetsky 1993) and the solar spectrum (Pickering et al. 1998). These applications necessitate the need for high-quality atomic data which accurately describe the processes of excitation and photoionization. This is further evidenced in SNe by following the nucleosynthesis decay path of $^{56}Ni \rightarrow {}^{56}Co \rightarrow {}^{56}Fe$, which occurs post explosion. Our principal aim is to facilitate modelling within the astrophysics community with accurate and up-to-date atomic transitions necessary for synthetic spectral analysis, allowing detailed comparisons to be carried out with observation. Stand-alone reports stress both the importance and absence of photon/electron interaction with systems of Iron, Cobalt and Nickel (Ruiz-Lapuente 1995; Hillier 2011; Dessart et al. 2014).

The photoionization cross-sections are to be implemented into the 3D plus time-dependent computer code ARTIS, which models the ejecta of Type Ia SNe as discussed in detail by Sim (2007); Kromer & Sim (2009). Currently, only hydrogenic approximations, or fits to the cross-sections are incorporated into the codes. It is our aim to provide ground and excited state contributions to all possible final states. The code is based on a similar approach by Lucy (2005), where methods for treatment of the transporting radiation, kinetic energies, and ionization energies are considered to compute light curves for particular models and symmetries.

The Opacity Project has been an invaluable source for such data, but is often limited when considering Fe-peak species (Cunto & Mendoza 1992; Cunto et al. 1993). These important Fe-peaks are difficult to investigate due to their open d-shell structure which gives rise to many hundreds of target states for each electronic configuration and typically thousands of closely coupled channels. Hence the target states require substantial configuration interaction expansions for their accurate representation. Fe II is one such challenging case where over the last decade calculations for this ion have grown in size, complexity and sophistication. Significant differences, however, are still observed in the resulting atomic data as can be seen by

* E-mail: ntyndall01@qub.ac.uk (NBT); c.ramsbottom@qub.ac.uk (CAR)

the latest two major evaluations for the electron-impact excitation of Fe II (Ramsbottom et al. 2007; Bautista et al. 2015). Factors of 2 to 3 disparity being the norm at the temperature of maximum abundance 10^4 K for many of the low-lying forbidden lines.

There have been a number of studies focused on essential atomic data between species of Co I-III concerning bound transitions. These include oscillator strengths for neutral Cobalt between 2276 and 9357 Å (Cardon et al. 1982), transition probabilities through a multiconfiguration approach for comparison with observed infrared spectra (Nussbaumer & Storey 1988), and also a relativistic Hartree–Fock approach between the lowest 47 levels of Co II (Quinet 1998). More recently, collision strengths and other radiative data have been calculated for Co II (Storey, Zeippen & Sochi 2016) and Co IV (Aggarwal et al. 2016). During the preparation of this work, it has come to our attention a detailed study of electron-impact excitation cross-sections for Co III conducted by Storey & Sochi (2016), which we shall compare with in Sections 2 and 3.

The early ion stages of, and even neutral Cobalt are clearly important as detailed in the literature. Early observations has shown strong Co II lines in η Carinae (Thackeray 1976), confirmed more recently by Zethson et al. (2001) to be unusually strong, and in the UV regime in ζ Oph (Snow, Weiler & Oegerle 1979), confirmed by Federman et al. (1993). These lines are apparent in the binary star HR5049 (Dworetsky, Trueman & Stickland 1980; Dworetsky 1982) – which previously have been unidentified due to the lack of laboratory data. In this same study, the amount of Cobalt is estimated to be around 3.0 dex overabundant relative to the Sun.

Due to the decay path of ^{56}Ni, Cobalt is often observed in various SNe at both early and late epochs. The Type II SNe 1987A, exploded in the large magellanic cloud, providing a study of the expanding ejecta as the ^{56}Co decays. A large proportion of Fe II and Co II lines are blended due to their similar ionization energies, but the strong 1.547 μm line occurs from the transition $a^5F_5 \rightarrow b^3F_4$ (Meikle et al. 1989; Li, McCray & Sunyaev 1993) in Co II. The Co III $a^4F_{9/2} \rightarrow a^2G_{9/2}$ 0.589 μm line in another Type II SNe, 1991bg, is used as a diagnostic to infer the mass of synthesized ^{56}Ni. It is also possible to deduce important properties such as the mass of the exploding star (Mazzali et al. 1997).

The Co II and Co III ions under discussion in this publication have also received much interest over the last decade. The mid-infrared spectrum of SNe 2003hv and 2005df show strong Co III line emissions and even emission from Co IV (Gerardy et al. 2007). However, the collisional processes included in the model have been approximated using statistically weighted collision strengths. A study of the near-infrared spectra from SNe 2005df yields strong Co III emission lines initially but by day 200 the majority of Cobalt has expectedly decayed down to Fe (Diamond, Hoeflich & Gerardy 2015). A number of Co III lines are still visible at late times for Type Ia SNe as documented in (Ruiz-Lapuente 1995). These lines would be extremely beneficial in particular diagnostic work, but as outlined above, little collisional data exists. In addition the photoionization cross-sections employed in the models are obtained from a central potential approximation (Reilman & Manson 1979) for the ground state only. Co III is also present in SNe 2014J and the 11.888 μm line is useful for monitoring the time evolution of the photosphere, and again, the mass of synthesized Ni (Telesco et al. 2015). It is evident from these works and the associated applications the importance of conducting sophisticated and complete calculations for the lowly ionized Fe-peak species of Fe, Ni and Co.

In Section 2, we discuss the development of an accurate structure model for Co III to include in the *R*-matrix collisional calculations for electron-impact excitation and photoionization. The accuracy of this model will be tested by reassessing energy levels of the target states and the conformity of transition probabilities with previous assessments. In Section 3, we present level-resolved ground and excited state photoionization cross-sections for Co II and a selection of collision strengths and effective collision strengths for the electron-impact excitation of Co III. Comparisons will be made where possible with existing data but these are limited. Finally we summarize our findings and conclusions in Section 4.

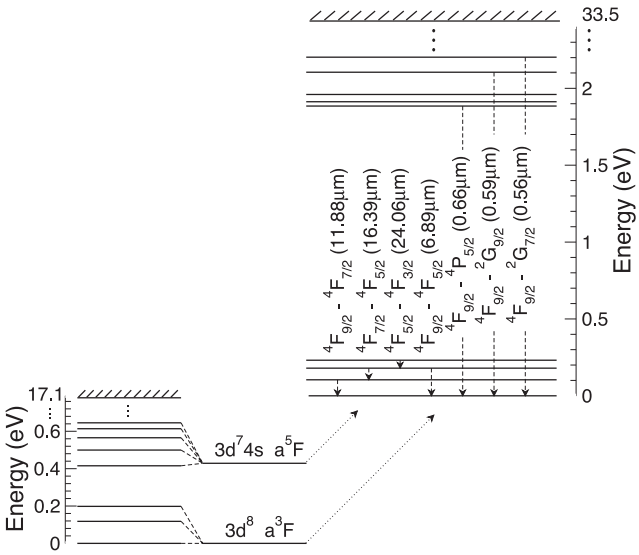

Figure 1. Important lines in the infrared and visible energy bands between levels of Co III amongst the $3d^7$ configuration and involving the ground term ^{4}F. The neighbouring system of Co II is to the left with its split *J* levels to indicate the photoionization process.

2 IMPORTANT TRANSITIONS FOR SYNTHETIC SPECTRAL MODELLING

This paper focuses initially on transitions that occur between discrete states of our atomic system, Co III. In Fig. 1, we graphically present some of the most important lines in the infrared and visible energy bands of the spectrum. Transitions among the ground state term ^{4}F and levels of the parent ion Co III with configuration $3d^7$ are shown on the right-hand side. The neighbouring system Co II is also shown on the left complete with its fine-structure split *J* levels to indicate the photoionization process under investigation.

2.1 Target description and bound state transitions

We first detail results obtained from transitions within the bound system of Co III and our *ab initio* energy eigenvalues. The Dirac–Coulomb Hamiltonian can be written as,

$$H_{\rm D} = \sum_{k=1}^{N} -{\rm i}c\boldsymbol{\alpha}\nabla_k + (\boldsymbol{\beta} - 1)c^2 - \frac{Z}{r_k} + \sum_{k<j}^{N} \frac{1}{|\mathbf{r}_j - \mathbf{r}_k|} \qquad (1)$$

which is then incorporated into the GRASP0 computer package. $\boldsymbol{\alpha}$ and $\boldsymbol{\beta}$ relates the Pauli spin matrices, c is the speed of light, $Z = 27$ is the atomic number and $N = 25$ is the number of electrons for the system.

As stated in the introduction, partially filled d-shell systems are difficult due to the hundreds of levels associated with a single configuration. Initially, we include three configurations, $3d^7$ and

Table 1. Energies for the lowest 50 levels of Co III are presented in eV relative to the ground state $3d^7\ a^4F_{9/2}$. *S&C* is from the work of Sugar & Corliss (1985). *model 1*, *model 2*, *model 3* are the current results from GRASP0 and the last column are the lowest 15 levels from Storey & Sochi (2016). We also present the per cent difference between our current *model 2* and *S&C* in the 6th column.

Index	Level	*S&C*	*Model 1*	*Model 2*	*Per cent*	*Model 3*	*Storey*
1	$3d^7\ a^4F_{9/2}$	0.000 00	0.000 00	0.000 00	0.0	0.000 00	0.000 00
2	$3d^7\ a^4F_{7/2}$	0.104 30	0.103 55	0.099 39	4.7	0.099 80	0.102 16
3	$3d^7\ a^4F_{5/2}$	0.179 94	0.180 01	0.172 55	4.1	0.173 21	0.177 05
4	$3d^7\ a^4F_{3/2}$	0.231 45	0.232 63	0.222 80	3.7	0.223 62	0.228 38
5	$3d^7\ a^4P_{5/2}$	1.884 80	2.394 05	2.204 36	16.9	2.197 61	2.293 69
6	$3d^7\ a^4P_{3/2}$	1.912 85	2.426 37	2.232 71	16.7	2.226 08	2.329 04
7	$3d^7\ a^4P_{1/2}$	1.960 36	2.472 83	2.278 75	16.2	2.272 44	2.370 33
8	$3d^7\ a^2G_{9/2}$	2.104 96	2.390 59	2.389 92	13.5	2.388 42	2.427 73
9	$3d^7\ a^2G_{7/2}$	2.202 73	2.489 67	2.482 50	12.7	2.481 38	2.523 95
10	$3d^7\ a^2P_{3/2}$	2.503 85	3.162 29	2.852 43	13.9	2.843 34	3.178 09
11	$3d^7\ a^2P_{1/2}$	2.593 56	3.270 65	2.964 28	14.3	2.956 73	3.282 36
12	$3d^7\ a^2H_{11/2}$	2.816 96	3.183 56	3.352 70	19.0	3.352 60	3.184 78
13	$3d^7\ a^2H_{9/2}$	2.905 48	3.268 36	3.431 16	18.1	3.431 43	3.270 58
14	$3d^7\ a^2_2D_{5/2}$	2.858 93	3.446 72	3.062 77	7.1	3.047 40	3.447 26
15	$3d^7\ a^2_2D_{3/2}$	3.004 98	3.603 58	3.231 40	7.5	3.218 73	3.599 63
16	$3d^7\ a^2_2F_{5/2}$	4.590 02	5.513 92	5.366 09	16.9	5.357 16	–
17	$3d^7\ a^2F_{7/2}$	4.626 66	5.558 37	5.408 63	16.9	5.399 98	–
18	$3d^64s\ a^6D_{9/2}$	5.757 62	6.708 46	6.068 49	5.4	6.201 78	–
19	$3d^64s\ a^6D_{7/2}$	5.827 64	6.789 42	6.146 50	5.5	6.279 25	–
20	$3d^64s\ a^6D_{5/2}$	5.878 76	6.848 69	6.203 78	5.5	6.336 14	–
21	$3d^64s\ a^6D_{3/2}$	5.913 87	6.889 47	6.243 24	5.5	6.375 36	–
22	$3d^64s\ a^6D_{1/2}$	5.934 48	6.913 40	6.266 43	5.6	6.398 40	–
23	$3d^64s\ a^4D_{7/2}$	6.909 54	8.420 15	7.722 55	11.8	8.049 98	–
24	$3d^64s\ a^4D_{5/2}$	6.989 46	8.512 85	7.811 96	11.8	8.138 68	–
25	$3d^64s\ a^4D_{3/2}$	7.041 66	8.573 68	7.870 84	11.8	8.197 22	–
26	$3d^64s\ a^4D_{1/2}$	7.071 67	8.608 77	7.904 80	11.8	8.230 95	–
27	$3d^7\ a^2_1D_{3/2}$	–	8.671 61	7.930 64	–	7.965 45	–
28	$3d^7\ a^2_1D_{5/2}$	–	8.610 18	8.001 19	–	7.893 75	–
29	$3d^64s\ b^4P_{5/2}$	8.794 71	10.250 65	9.638 34	9.6	9.809 74	–
30	$3d^64s\ a^4H_{13/2}$	8.880 14	10.001 20	9.382 43	5.6	9.553 49	–
31	$3d^64s\ a^4H_{11/2}$	8.911 21	10.031 98	9.412 43	5.6	9.583 37	–
32	$3d^64s\ a^4H_{9/2}$	8.937 19	10.058 05	9.437 86	5.6	9.608 83	–
33	$3d^64s\ a^4H_{7/2}$	8.960 40	10.080 57	9.459 63	5.6	9.630 75	–
34	$3d^64s\ b^4P_{3/2}$	8.969 26	10.465 63	9.845 80	9.8	10.017 10	–
35	$3d^64s\ b^4P_{1/2}$	9.077 44	10.594 39	9.970 61	9.8	10.140 09	–
36	$3d^64s\ b^4F_{9/2}$	9.086 31	10.423 02	9.810 43	8.0	9.981 84	–
37	$3d^64s\ b^4F_{7/2}$	9.117 82	10.460 16	9.846 05	8.0	10.016 92	–
38	$3d^64s\ b^4F_{5/2}$	9.140 93	10.491 01	9.875 66	8.0	10.046 24	–
39	$3d^64s\ b^4F_{3/2}$	9.157 70	10.515 40	9.898 93	8.1	10.069 29	–
40	$3d^64s\ a^4G_{11/2}$	9.487 14	10.772 37	10.159 94	7.1	10.335 33	–
41	$3d^64s\ b^2P_{3/2}$	9.520 88	11.328 10	10.679 64	12.2	10.964 74	–
42	$3d^64s\ a^4G_{9/2}$	9.561 80	10.852 46	10.237 81	7.1	10.408 98	–
43	$3d^64s\ a^4G_{7/2}$	9.594 28	10.886 42	10.271 10	7.0	10.441 58	–
44	$3d^64s\ b^2H_{11/2}$	9.597 82	11.049 02	10.397 01	8.3	10.678 36	–
45	$3d^64s\ a^4G_{5/2}$	9.605 34	10.895 26	10.280 19	7.0	10.451 25	–
46	$3d^64s\ b^2P_{1/2}$	9.724 61	11.570 42	10.915 82	12.2	11.197 12	–
47	$3d^64s\ b^2H_{9/2}$	9.624 02	11.082 83	10.429 07	8.4	10.713 76	–
48	$3d^64s\ b^2F_{7/2}$	9.785 80	11.447 78	10.802 18	10.4	11.085 48	–
49	$3d^64s\ b^2F_{5/2}$	9.847 49	11.533 72	10.882 86	10.5	11.168 01	–
50	$3d^64s\ b^2G_{9/2}$	10.211 75	11.831 44	11.184 70	9.6	11.470 76	–

$3d^6$[4s, 4p] during the optimization process, denoted as *model 1*, which results in a total of 262 fine structure levels to describe the Co III ion. The ground state of which is $3d^7a^4F_{9/2}$. Next we optimize all orbitals up to 3d on the configurations from the double electron promotions, $3s^2$, $3p^2 \rightarrow 3d^2$ and include in the total calculation all configurations from *model 1* plus $3p^63d^9$ (double promotion from 3s to 3d) and $3s^23p^43d^9$ (double promotion from 3p to 3d). This technique can be useful as it alleviates the necessity to include numerous pseudo-states into the calculation. We denote this *model 2* which constitutes a total of 292 levels. Finally, by including $3d^5$[$4s^2$, $4p^2$] and $3d^54s4p$, the number of levels drastically increases to 1259 levels, and we label this as *model 3*.

We present in Table 1 our *ab initio* energy levels obtained from GRASP0 in eV for the lowest lying 50 levels alongside those observed by Sugar & Corliss (1985). We also present the per cent difference between Sugar & Corliss (1985) and our *model 2*, and also provide the lowest 15 levels of Storey & Sochi (2016). Good agreement is found (<10 per cent for the majority of levels) between the

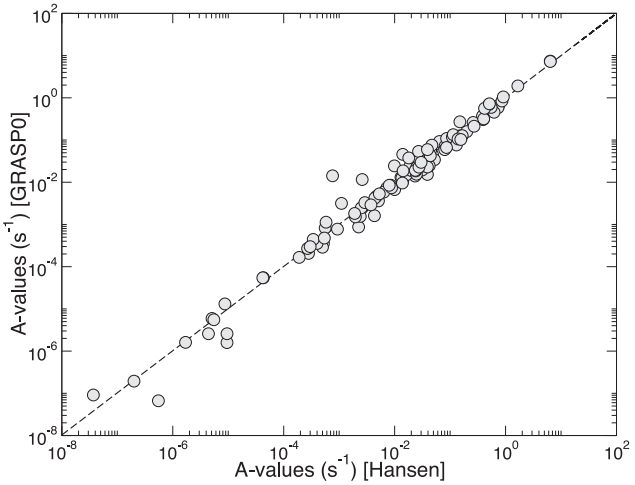

Figure 2. Present theoretical *A*-values after the scaling factors in equation (2) have been applied, plotted against the results of Hansen et al. (1984) in s^{-1} on a log/log scale.

present *model 2* and *model 3* energies and those of Storey & Sochi (2016). As with other Fe-peak ions, the energy levels of the lowest-lying $3d^7$ fine-structure states are notoriously difficult to determine. The highest disparities are found for these levels when compared with Sugar & Corliss (1985), the largest being for the $3d^7\ ^4F_{9/2} \rightarrow 3d^7\ ^2H_{11/2}$ (1-12) transition. For levels indexed above 17 the differences are at most 10 to 11 per cent and for many levels by considerably less. The main problem is due to the fact that a single 3d orbital is used to describe the configuration state functions for multiple configurations of type $3d^7$ and $3d^64s$. Similar differences were reported by Ramsbottom (2009) for the low-lying $3d^7$ fine-structure levels of Fe II. Despite the high per cent differences found between these lowest levels in Table 1, overall the average per cent change across the 171 Sugar & Corliss (1985) $J\pi$ symmetries is a more acceptable 6.2 per cent. The differences between *model 2* and *model 3* are not significant enough to justify the much larger calculation, and we can also benefit by employing all 292 levels into the close-coupling wavefunction expansion of the Co III. We therefore adopt our *model 2* as the final model for the scattering calculation.

The *A*-value, or transition probability, can be calculated at this stage of the calculation. It is a direct measure of the line strength between two states of our system, and we therefore require accurate wavefunctions and energies. We can account for the discrepancy between GRASP0 and Sugar & Corliss (1985) energy states by considering the following multiplicative scaling factor,

$$\left(\frac{\Delta E_{ji}^{\rm expt}}{\Delta E_{ji}^{\rm theo}}\right)^{\eta}. \qquad (2)$$

Here we set $\eta = 3$ or $\eta = 5$ for electric and magnetic dipole or quadrupole transitions between two states j and i. It is found that these are shifted by a fraction of the recorded values. A procedure through a least-squares fitting process (Cowan 1981) is the most commonly implemented source of *A*-values for this ion stage of Cobalt (Hansen, Raassen & Uylings 1984) to date. A total of 130 forbidden transitions within this $3d^7$ complex are reported, and are provided for comparison in Fig. 2 against our results after the scaling in equation (2) has been performed. The *A*-values are presented on a logarithmic versus logarithmic scale to incorporate the various

Table 2. *A*-values from Fivet, Quinet & Bautista (2016), Hansen et al. (1984), our current *model 2* after the multiplicative scaling factors in equation (2) have been applied and results from Storey for transitions amongst the lowest 7 levels.

$i-j$	*Fivet*	*Hansen*	*Model 2*	*Storey*
1 – 2	2.00×10^{-2}	2.00×10^{-2}	2.00×10^{-2}	2.00×10^{-2}
1 – 3	–	1.80×10^{-9}	1.75×10^{-9}	–
1 – 5	6.65×10^{-2}	4.80×10^{-2}	4.53×10^{-2}	5.55×10^{-2}
2 – 3	1.31×10^{-2}	1.30×10^{-2}	1.31×10^{-2}	1.31×10^{-2}
2 – 4	–	5.90×10^{-10}	5.70×10^{-10}	–
2 – 5	1.78×10^{-2}	1.35×10^{-2}	1.26×10^{-2}	1.51×10^{-2}
2 – 6	3.73×10^{-2}	2.70×10^{-2}	2.58×10^{-2}	3.14×10^{-2}
3 – 4	4.63×10^{-3}	4.70×10^{-3}	4.63×10^{-3}	4.63×10^{-3}
3 – 5	–	2.60×10^{-3}	2.45×10^{-3}	3.14×10^{-3}
3 – 6	2.21×10^{-2}	1.63×10^{-2}	1.50×10^{-2}	1.85×10^{-2}
3 – 7	2.73×10^{-2}	2.00×10^{-2}	1.89×10^{-2}	2.30×10^{-2}
4 – 5	–	4.00×10^{-4}	3.55×10^{-4}	–
4 – 6	–	4.40×10^{-3}	4.22×10^{-3}	5.14×10^{-3}
4 – 7	3.60×10^{-2}	2.60×10^{-2}	2.47×10^{-2}	3.02×10^{-2}
5 – 6	–	2.70×10^{-4}	2.69×10^{-4}	–
5 – 7	–	5.50×10^{-9}	5.20×10^{-9}	–
6 – 7	–	2.50×10^{-3}	2.47×10^{-3}	2.45×10^{-3}

magnitudes of results. To investigate this comparison more closely, we present in Table 2 a selection of transitions among the lowest 7 levels of Co III. Comparisons are made between the values of Hansen et al. (1984), the present *model 2* with scaled transition energy levels and the recent results from Storey & Sochi (2016). Excellent agreement is evident for the bulk of the transitions considered with the greatest difference of 12.7 per cent occurring for the $3d^7a^4F_{3/2}$–$3d^7a^4P_{5/2}$ (4–5) transition.

A much larger calculation for doubly ionized Fe-peak species has been performed recently by Fivet et al. (2016) using the same suite of codes as Hansen et al. (1984), and also by considering the computer package AUTOSTRUCTURE, (Eissner, Jones & Nussbaumer 1974; Badnell 1986), where the optimization process is carried out with a Thomas–Fermi–Dirac potential using lambda scaling parameters. Numerous doubly ionized ions of Fe, Ni and Co were considered in this publication. Single and double electron promotions out of the 3d, and also single electron promotions out of the 3s to the 5s orbital were included and comprised the basis expansion for both calculations. This is the most sophisticated and complete report for radiative rates in Co III to date. Within the $3d^7$ complex, we vary approximately 27 per cent on average compared with both methods of Fivet et al. (2016).

2.2 The *R*-matrix method

To extend this problem to include interactions with photons and electrons, we consider the *R*-matrix method. A general overview of the theory can be found in Burke (2011). The theory was developed to perform electron scattering by Burke, Hibbert & Robb (1971) and extended for photoionization by Burke & Taylor (1975).

These calculations can be performed using a non-orthogonal B-spline basis set approach (Zatsarinny & Froese Fischer 2000; Zatsarinny & Bartschat 2004), intermediate-coupling frame transformation methods (Griffin, Badnell & Pindzola 1998) and one-body perturbation corrections to the non-relativistic Hamiltonian via the Breit–Pauli operators (Scott & Burke 1980) to name a few. In this paper, we consider the Dirac atomic *R*-matrix codes (DARC) which includes relativistic effects through the Dirac Hamiltonian in equation (1) for this mid to heavy species ion. The

wavefunctions obtained from GRASP0 are formatted suitable for inclusion into DARC. Validity of these methods between the outlined theoretical approaches are always important, and enhance the robustness of the techniques carried out as seen in Tyndall et al. (2016) for Ar^+ and Fernández-Menchero, Del Zanna & Badnell (2015) for Al^{9+}. Therefore, it is possible to benchmark sophisticated experimental techniques against theory (Müller et al. 2009; Gharaibeh et al. 2011).

2.3 Photoionization

The photoionization process is described by,

$$h\nu + \mathrm{Co}^+ \{3\mathrm{d}^8\mathrm{a}^3\mathrm{F}^\mathrm{e}_J, 3\mathrm{d}^7 4\mathrm{s}\ \mathrm{a}^5\mathrm{F}^\mathrm{e}_J\} \rightarrow \mathrm{Co}^{2+} + e^-, \quad (3)$$

where a photon leads to the ionization of an electron directly, or via a Rydberg resonance. The process in equation (3) can be formally calculated as,

$$\sigma^\mathrm{p}_{i\rightarrow j} = \frac{4\pi a_0^2 \alpha\omega}{3g_i} \sum (\Psi_j||\mathbf{D}||\Psi_i)$$

for initial and final scattering wavefunctions subject to the total dipole contribution. $\omega = h\nu$ is the photon energy or $\omega \rightarrow \omega^{-1}$ when considering the velocity operator, **D**. α is the fine structure constant, a_0 is the Bohr radius and g_i is the statistical weight of the initial state wavefunction. The summation is then carried out over all dipole-allowed transitions. The total wavefunctions Ψ are obtained from the momenta couplings with those wavefunctions obtained in Section 2.1. We represent these σ^p in units of Mb ($\equiv 10^{-18}\mathrm{cm}^2$) throughout this work.

The transitions of interest are calculated within the lowest eight fine-structure levels of Co II pertaining to the two $LS\pi$ states as noted in equation (3). We also maintain a closed $3p^6$ core and are only concerned with low-energy transitions above threshold. Therefore, all even and odd allowed dipole symmetries up to $J = 6$ are calculated subject to the selection rules.

2.4 Electron-impact excitation

The collision strength between an initial state i and final state j can be obtained from the cross-section, σ^e,

$$\Omega_{i\rightarrow j} = \frac{g_i k_i^2}{\pi a_0^2} \sigma^e_{i\rightarrow j}. \quad (4)$$

These collision strengths represent a detailed spectrum, complete with the already mentioned auto-ionizing states. To present the results in a more concise format, we assume a Maxwellian distribution of the colliding electron velocities. We define the effective collision strength as

$$\Upsilon_{i\rightarrow j} = \int_0^\infty \Omega_{i\rightarrow j} \mathrm{e}^{-\epsilon_f/kT} \mathrm{d}\left(\frac{\epsilon_f}{kT}\right), \quad (5)$$

where ϵ_f is the ejected energy of the electron, $3800 \leq T \leq 40\,000$ in K, and $k = 8.617 \times 10^{-5}$ eV K^{-1} is the Boltzmann constant. Each $\Upsilon_{i\rightarrow j}$ is calculated for 11 electron temperatures.

We calculate the main contribution to the collision strength defined in equation (4) from the partial waves up to $J = 13$ of both even and odd parity. These are obtained by considering appropriate total multiplicity and orbital angular momentum partial waves. However, in order to converge transitions at higher energies, we explicitly calculate partial waves up to $J = 38$ and use top-up procedures outlined in Burgess (1974) to account for further contribution to the total cross-section. The collision strengths can be extended to high-energy limits through an interpolation technique described by Burgess & Tully (1992).

Table 3. Bound state energies of the lowest eight states of Co II relative to the ground state $3d^7\ a^3F_{9/2}$ of Co III compared with the relative energies of Pickering et al. (1998), labelled as *Pickering*.

Index	Level	*Pickering*	*Current*	Δ
1	$3p^6 3d^8\ a^3F_4$	−17.0844	−16.6232	0.46
2	$3p^6 3d^8\ a^3F_3$	−16.9666	−16.5004	0.47
3	$3p^6 3d^8\ a^3F_2$	−16.8864	−16.4159	0.47
4	$3p^6 3d^7(^4F)4s\ a^5F_5$	−16.6690	−16.3531	0.32
5	$3p^6 3d^7(^4F)4s\ a^5F_4$	−16.5849	−16.2694	0.32
6	$3p^6 3d^7(^4F)4s\ a^5F_3$	−16.5189	−16.2031	0.32
7	$3p^6 3d^7(^4F)4s\ a^5F_2$	−16.4707	−16.1544	0.32
8	$3p^6 3d^7(^4F)4s\ a^5F_1$	−16.4391	−16.1224	0.32

3 RESULTS

As mentioned previously, the photoionization of Co II and electron-impact excitation of Co III rely on an accurate description of the Co III wavefunctions. We are able to retain consistency throughout the calculation, and the fundamental *R*-matrix conditions apply to both processes. We select a total of 14 continuum basis orbitals per angular momenta to describe the scattered electron. The *R*-matrix boundary is then set at 10.88 au in order to enclose the radial extent of the 4p orbital. To make comparisons between observation, the target thresholds obtained in Table 1 have been shifted to those of Sugar & Corliss (1985).

3.1 Photoionization

In this section, we detail our results from the photoionization process described by equation (3). There is minimal atomic data for this interaction in the literature as only the total ground state transition exists. The first compilation is from Reilman & Manson (1979), using Hartree–Slater wavefunctions from a central field potential. Secondly, and more recently, Verner et al. (1993) have calculated cross-sections using the Hartree–Dirac–Slater potential and then applying an analytic fitting procedure. Recently, the Los Alamos suite of codes by Fontes et al. (2015) have been used to obtain results by a distorted wave method. For this we look at the photoionization of a 3d electron into the configuration averaged final states. To carefully resolve these spectra, we have employed a total of 200 000 equally spaced energy points over a photoelectron energy range of 20 eV. This ensures the high *nl* Rydberg resonant states are properly delineated.

The initial bound states that are required, corresponding to the left-hand side of equation (3) are calculated first. In Table 3, we present the energies relative to the ground state $3d^7\ a^3F_{9/2}$ of Co III from our current *R*-matrix results and compare with those of Pickering et al. (1998). We deviate ≈0.47 eV for the $3d^8$ and ≈0.32 eV for the $3d^7(^4F)4s$. Despite these discrepancies good agreement is evident for the splitting between all eight fine-structure levels.

In Fig. 3, we present the photoionization cross-section representing the statistically weighted initial state $3d^8\ a^3F$ to all allowed final states. The results in this figure have been convoluted with a 10 meV Gaussian profile at full-width at half-maximum to better compare with experiment. We directly compare here with the results of all three previously mentioned theoretical methods (Reilman & Manson 1979; Verner et al. 1993; Fontes et al. 2015). These methods

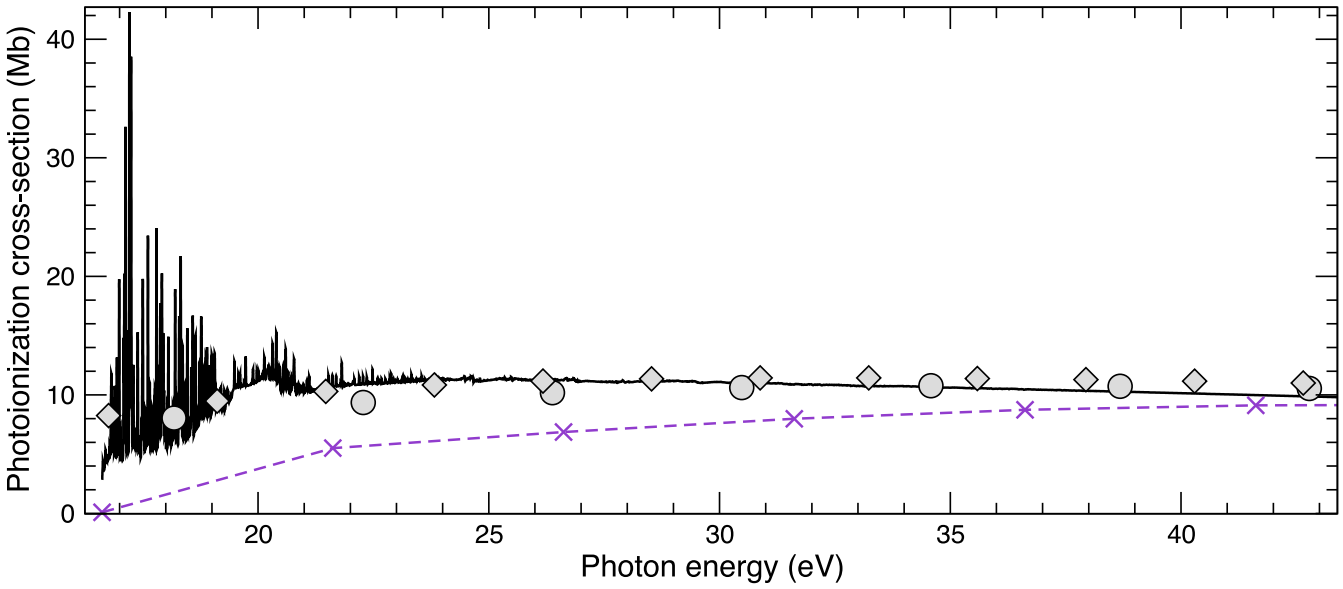

Figure 3. Photoionization cross-sections in Mb against the photon energy in eV. The solid black curve is the total initial ground state, statistically weighted $3d^8\ ^3F$ to all allowed dipole final states. The crosses are results from Reilman & Manson (1979), the diamonds are from Verner et al. (1993), and finally the circles are those from the distorted wave calculation. (Fontes et al. 2015)

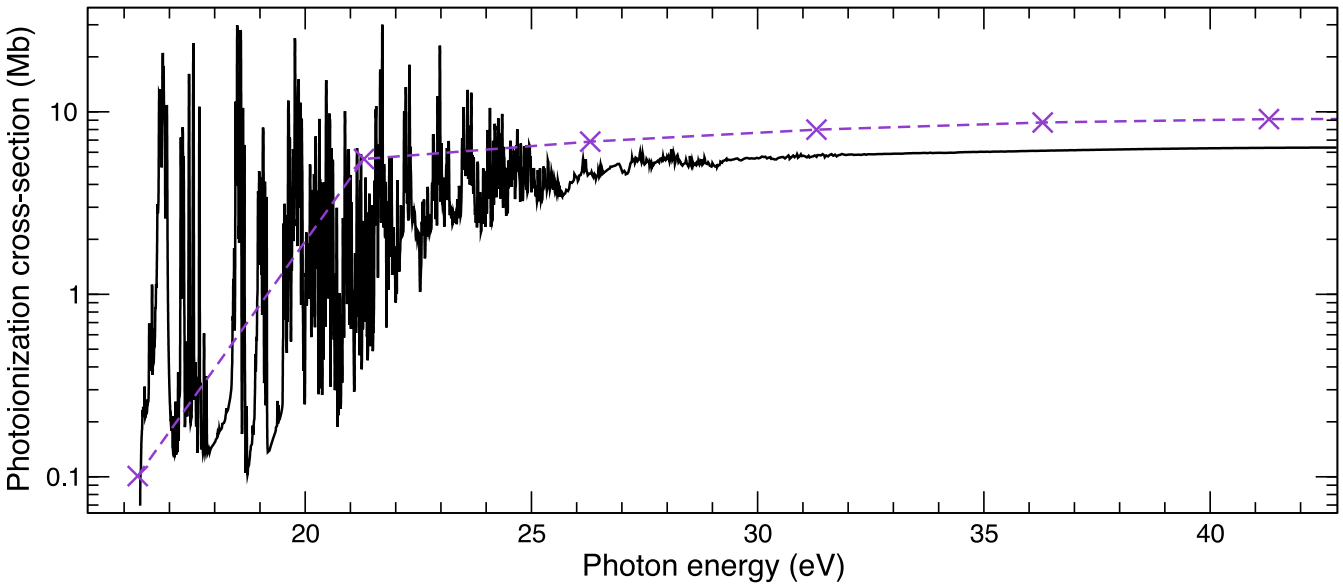

Figure 4. Photoionization cross-sections in Mb against the photon energy in eV. The solid black curve is the photoionization, statistically averaged levels of $3d^7 4s\ ^5F$ to all allowed dipole final states. The crosses are results from Reilman & Manson (1979).

do not include auto-ionization states and therefore only background cross-sections are presented. It is clear however that the results are in excellent agreement, with only Reilman & Manson (1979) reaching factors of 2 or more difference in the <20 eV region. As over 200 eigenenergies obtained from GRASP0 are < 28 eV of photon energy, this above threshold region is dominated by multiple Rydberg resonances series converging on to these states.

The second statistically weighted bound state a^5F of Co II is from the configuration $3d^7 4s$. In Fig. 4, we present the total photoionization cross-section for this metastable level and compare with the earlier work of Reilman & Manson (1979). This cross-section is weighted as a consequence of its five fine-structure split levels $1 < J < 5$. Again, the photoionization of the 3d electron is favourable, so we expect the majority of the spectrum to be accounted for from the $3d^6 4s$ target states, which are accessible at 5.757 62 eV above the ionization threshold. Good agreement is found between the two calculations for the background cross-section, particularly in the higher photon energy range above 25 eV.

3.2 Electron-impact excitation

The procedures outlined in Section 2.4 are now applied to obtain accurate collision strengths and the corresponding effective collision strengths describing the electron-impact excitation of Co III. There has been work carried out recently on both singly ionized Co II (Storey et al. 2016) and also Co III (Storey & Sochi 2016). The work of Storey & Sochi (2016) is similar to our current evaluation,

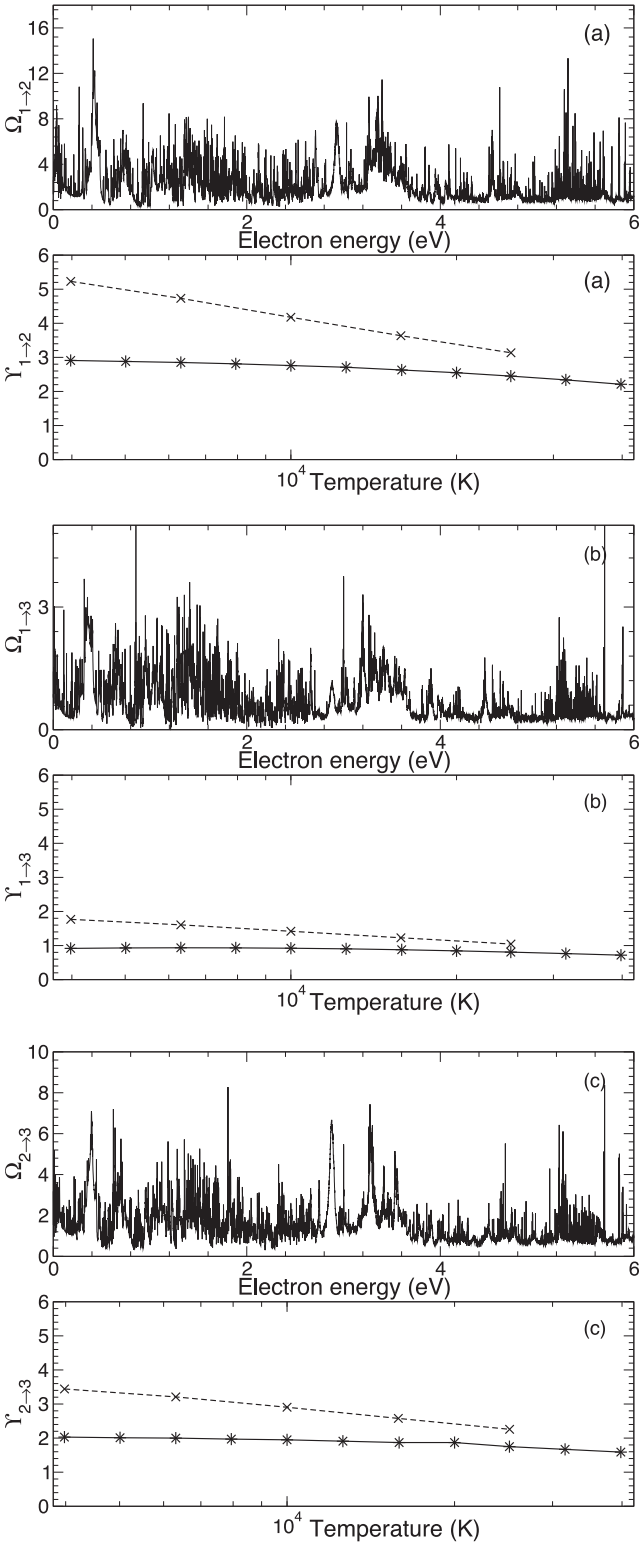

Figure 5. The collision strengths, (a) $\Omega_{1\rightarrow2}$, (b) $\Omega_{1\rightarrow3}$ and (c) $\Omega_{2\rightarrow3}$ presented as a function of electron energy in eV. Also presented are the corresponding effective collision strengths as a function of temperature in K. Solid black lines with stars are the current data set and the dashed line with crosses represent the results from Storey & Sochi (2016).

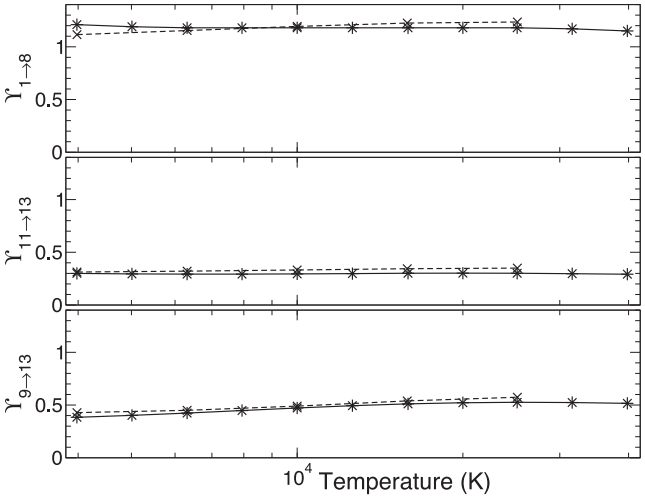

Figure 6. The effective collision strengths, $\Upsilon_{1\rightarrow8}$ (top), $\Upsilon_{11\rightarrow13}$ (middle) and $\Upsilon_{9\rightarrow13}$ (bottom), presented as a function of temperature in K (bottom). Solid black lines with stars are the current data set and the dashed line with crosses represent the results from Storey & Sochi (2016).

but differences are evident in the method considered. Their basis set has been optimized using AUTOSTRUCTURE, and also includes a $4\bar{d}$ orbital plus additional configuration interaction. However, only a total of 109 fine structure levels have been included in the close coupling target representation. The semi-relativistic Breit–Pauli *R*-matrix approach was considered during the scattering calculation.

It is necessary to obtain a level of convergence in the spectra of collision strengths by applying a mesh with incremental step sizes in electron energy until convergence is achieved. Initially 5000 equally spaced energy points were considered and it was found by the time we had reached 40 000 energy points, the effective collision strengths had converged for the forbidden transitions among the 292 levels. To extend the energy region we incorporated an additional coarse mesh above the last valence threshold. Due to the long-range nature of the Coulomb potential further contributions to the collision strengths arise from the higher partial waves, particularly for the dipole allowed lines. We compute these additional contributions using the Burgess (1974) sum rule as well as a geometric series for the long-range non-dipole transitions. Hence converged total collision strengths were accurately generated for all 42 486 transitions among the 292 fine-structure levels included in the collision calculation. The corresponding effective collision strengths were obtained by averaging these finely resolved collision strengths over a Maxwellian distribution of electron velocities for electron temperatures ranging from 3800 to 40 000 K.

We present in Fig. 5 the resulting collision strengths and effective collision strengths for a selection of the forbidden near-infrared transitions involving the fine-structure split levels of the ^{4}F ground state of Co III. Panel (a) represents transition from level 1→ 2, panel (b) 1 → 3, and panel (c) 2 → 3. The collision strength is strongest here for the $\Omega_{1\rightarrow2}$ transition due to the $\Delta J = 0$ partial wave.

Comparison of the effective collision strengths are made for each transition with the work of Storey & Sochi (2016) and good agreement is found for all temperatures above 10 000 K. For temperatures below this value the two calculations deviate somewhat, most probably due to the differing resonance profiles converging on to differing threshold positions. The present calculation has shifted the thresholds to lie in their exact observed positions listed in Table 1. In Fig. 6 we present the effective collision strengths for some higher

Table 4. Effective collision strengths as defined by equation (5) are presented between an upper (j) and lower state (i), across a range of nine temperatures (K), $3800 < T < 25\,100$ K. We have denoted $(a) \equiv \times 10^a$.

i	j	log T (K) 3.6	3.7	3.8	3.9	4	4.1	4.2	4.3	4.4
1	2	2.92(0)	2.90(0)	2.86(0)	2.82(0)	2.77(0)	2.70(0)	2.63(0)	2.54(0)	2.44(0)
1	3	9.24(−1)	9.36(−1)	9.41(−1)	9.37(−1)	9.26(−1)	9.06(−1)	8.79(−1)	8.45(−1)	8.06(−1)
2	3	2.02(0)	2.01(0)	1.99(0)	1.97(0)	1.94(0)	1.91(0)	1.86(0)	1.81(0)	1.74(0)
1	4	3.17(−1)	3.23(−1)	3.26(−1)	3.25(−1)	3.21(−1)	3.13(−1)	3.03(−1)	2.90(−1)	2.75(−1)
2	4	7.46(−1)	7.65(−1)	7.77(−1)	7.80(−1)	7.76(−1)	7.64(−1)	7.43(−1)	7.17(−1)	6.85(−1)
3	4	1.42(0)	1.42(0)	1.42(0)	1.42(0)	1.40(0)	1.39(0)	1.36(0)	1.32(0)	1.28(0)
1	5	1.16(0)	1.16(0)	1.17(0)	1.19(0)	1.20(0)	1.21(0)	1.21(0)	1.20(0)	1.19(0)
2	5	8.11(−1)	8.03(−1)	8.02(−1)	8.07(−1)	8.13(−1)	8.17(−1)	8.15(−1)	8.05(−1)	7.89(−1)
3	5	5.72(−1)	5.60(−1)	5.53(−1)	5.51(−1)	5.50(−1)	5.48(−1)	5.43(−1)	5.33(−1)	5.19(−1)
4	5	3.68(−1)	3.51(−1)	3.37(−1)	3.27(−1)	3.20(−1)	3.13(−1)	3.06(−1)	2.98(−1)	2.88(−1)
1	6	4.84(−1)	4.82(−1)	4.84(−1)	4.90(−1)	4.95(−1)	4.98(−1)	4.97(−1)	4.91(−1)	4.82(−1)
2	6	5.54(−1)	5.52(−1)	5.53(−1)	5.56(−1)	5.60(−1)	5.61(−1)	5.58(−1)	5.52(−1)	5.41(−1)
3	6	4.55(−1)	4.51(−1)	4.51(−1)	4.54(−1)	4.57(−1)	4.59(−1)	4.57(−1)	4.52(−1)	4.44(−1)
4	6	2.92(−1)	2.88(−1)	2.89(−1)	2.92(−1)	2.96(−1)	3.00(−1)	3.02(−1)	3.00(−1)	2.96(−1)
5	6	6.14(−1)	6.15(−1)	6.21(−1)	6.31(−1)	6.44(−1)	6.59(−1)	6.73(−1)	6.82(−1)	6.87(−1)
1	7	1.86(−1)	1.85(−1)	1.85(−1)	1.86(−1)	1.87(−1)	1.86(−1)	1.84(−1)	1.81(−1)	1.76(−1)
2	7	2.03(−1)	2.03(−1)	2.06(−1)	2.10(−1)	2.15(−1)	2.18(−1)	2.19(−1)	2.18(−1)	2.14(−1)
3	7	2.34(−1)	2.36(−1)	2.39(−1)	2.43(−1)	2.48(−1)	2.51(−1)	2.53(−1)	2.52(−1)	2.48(−1)
4	7	2.19(−1)	2.20(−1)	2.22(−1)	2.26(−1)	2.29(−1)	2.31(−1)	2.32(−1)	2.31(−1)	2.28(−1)
5	7	2.43(−1)	2.45(−1)	2.49(−1)	2.56(−1)	2.65(−1)	2.75(−1)	2.85(−1)	2.93(−1)	2.98(−1)
6	7	2.73(−1)	2.72(−1)	2.72(−1)	2.74(−1)	2.76(−1)	2.79(−1)	2.81(−1)	2.83(−1)	2.82(−1)
1	8	1.22(0)	1.20(0)	1.19(0)	1.19(0)	1.19(0)	1.19(0)	1.19(0)	1.19(0)	1.18(0)
2	8	7.27(−1)	7.14(−1)	7.06(−1)	7.02(−1)	6.99(−1)	6.98(−1)	6.96(−1)	6.92(−1)	6.86(−1)
3	8	3.85(−1)	3.76(−1)	3.70(−1)	3.65(−1)	3.62(−1)	3.59(−1)	3.55(−1)	3.51(−1)	3.45(−1)
4	8	1.75(−1)	1.69(−1)	1.65(−1)	1.60(−1)	1.57(−1)	1.53(−1)	1.50(−1)	1.46(−1)	1.43(−1)
5	8	3.24(−1)	3.18(−1)	3.11(−1)	3.07(−1)	3.04(−1)	3.02(−1)	3.01(−1)	3.00(−1)	2.98(−1)
6	8	1.56(−1)	1.51(−1)	1.47(−1)	1.43(−1)	1.41(−1)	1.40(−1)	1.39(−1)	1.38(−1)	1.37(−1)
7	8	5.48(−2)	5.20(−2)	4.93(−2)	4.70(−2)	4.51(−2)	4.36(−2)	4.24(−2)	4.14(−2)	4.03(−2)
1	9	3.16(−1)	3.10(−1)	3.06(−1)	3.05(−1)	3.05(−1)	3.04(−1)	3.03(−1)	3.01(−1)	2.97(−1)
2	9	5.02(−1)	4.99(−1)	4.99(−1)	5.01(−1)	5.05(−1)	5.08(−1)	5.11(−1)	5.12(−1)	5.10(−1)
3	9	5.33(−1)	5.29(−1)	5.29(−1)	5.31(−1)	5.34(−1)	5.37(−1)	5.40(−1)	5.41(−1)	5.39(−1)
4	9	4.29(−1)	4.27(−1)	4.26(−1)	4.27(−1)	4.29(−1)	4.32(−1)	4.33(−1)	4.34(−1)	4.32(−1)
5	9	1.53(−1)	1.46(−1)	1.41(−1)	1.37(−1)	1.36(−1)	1.36(−1)	1.36(−1)	1.37(−1)	1.36(−1)
6	9	1.72(−1)	1.66(−1)	1.62(−1)	1.58(−1)	1.56(−1)	1.56(−1)	1.55(−1)	1.55(−1)	1.55(−1)
7	9	1.09(−1)	1.06(−1)	1.04(−1)	1.02(−1)	1.01(−1)	9.99(−2)	9.95(−2)	9.92(−2)	9.86(−2)
8	9	1.29(0)	1.27(0)	1.26(0)	1.26(0)	1.27(0)	1.28(0)	1.29(0)	1.29(0)	1.28(0)
1	10	3.06(−1)	3.04(−1)	3.04(−1)	3.03(−1)	3.03(−1)	3.02(−1)	3.00(−1)	2.99(−1)	2.97(−1)
2	10	2.76(−1)	2.79(−1)	2.82(−1)	2.86(−1)	2.88(−1)	2.89(−1)	2.87(−1)	2.83(−1)	2.78(−1)
3	10	2.05(−1)	2.09(−1)	2.13(−1)	2.18(−1)	2.21(−1)	2.21(−1)	2.20(−1)	2.16(−1)	2.10(−1)
4	10	1.29(−1)	1.32(−1)	1.36(−1)	1.40(−1)	1.43(−1)	1.43(−1)	1.42(−1)	1.39(−1)	1.34(−1)
5	10	2.85(−1)	2.84(−1)	2.86(−1)	2.89(−1)	2.92(−1)	2.95(−1)	2.95(−1)	2.93(−1)	2.89(−1)
6	10	2.29(−1)	2.27(−1)	2.27(−1)	2.29(−1)	2.31(−1)	2.32(−1)	2.31(−1)	2.29(−1)	2.25(−1)
7	10	9.14(−2)	9.23(−2)	9.39(−2)	9.56(−2)	9.69(−2)	9.75(−2)	9.72(−2)	9.60(−2)	9.40(−2)
8	10	4.12(−1)	4.06(−1)	4.01(−1)	3.99(−1)	3.99(−1)	4.00(−1)	4.03(−1)	4.07(−1)	4.09(−1)
9	10	3.20(−1)	3.17(−1)	3.17(−1)	3.20(−1)	3.26(−1)	3.34(−1)	3.42(−1)	3.47(−1)	3.50(−1)
1	11	8.09(−2)	8.03(−2)	8.01(−2)	8.02(−2)	8.05(−2)	8.08(−2)	8.09(−2)	8.08(−2)	8.03(−2)
2	11	1.09(−1)	1.10(−1)	1.11(−1)	1.11(−1)	1.12(−1)	1.12(−1)	1.12(−1)	1.11(−1)	1.09(−1)
3	11	1.16(−1)	1.19(−1)	1.22(−1)	1.26(−1)	1.28(−1)	1.29(−1)	1.28(−1)	1.27(−1)	1.24(−1)
4	11	9.23(−2)	9.71(−2)	1.02(−1)	1.07(−1)	1.11(−1)	1.13(−1)	1.13(−1)	1.11(−1)	1.08(−1)
5	11	7.49(−2)	7.54(−2)	7.66(−2)	7.83(−2)	8.00(−2)	8.14(−2)	8.23(−2)	8.23(−2)	8.14(−2)
6	11	8.77(−2)	8.98(−2)	9.27(−2)	9.61(−2)	9.93(−2)	1.02(−1)	1.04(−1)	1.04(−1)	1.03(−1)
7	11	6.77(−2)	6.93(−2)	7.18(−2)	7.45(−2)	7.70(−2)	7.88(−2)	7.96(−2)	7.94(−2)	7.81(−2)
8	11	1.98(−1)	1.90(−1)	1.85(−1)	1.81(−1)	1.79(−1)	1.78(−1)	1.78(−1)	1.79(−1)	1.79(−1)
9	11	2.06(−1)	2.01(−1)	1.99(−1)	1.99(−1)	2.00(−1)	2.03(−1)	2.07(−1)	2.11(−1)	2.14(−1)
10	11	3.32(−1)	3.24(−1)	3.19(−1)	3.17(−1)	3.17(−1)	3.17(−1)	3.16(−1)	3.14(−1)	3.09(−1)

lying transitions, the $3d^7\ ^4F_{9/2}$–$3d^7\ ^2G_{9/2}$ ($1 \rightarrow 8$), $3d^7\ ^2P_{1/2}$–$3d^7\ ^2H_{9/2}$ ($11 \rightarrow 13$) and $3d^7\ ^2G_{7/2}$–$3d^7\ ^2H_{9/2}$ ($9 \rightarrow 13$). Excellent agreement is evident for all three transitions when a comparison is made with the data of Storey & Sochi (2016) across all temperatures where a comparison is possible. The collision strengths and effective collision strengths for all 42 486 forbidden and allowed lines are available from the authors on request but we present in Table 4 the effective collision strengths for all transitions among

Table 5. Emissivities relative to H β for a select number of transitions. The results are from our *Present* calculation and those presented in Storey & Sochi (2016) for two electron densities at one temperature, $T = 10\,000$ K.

	$\rho\,(N_e = 10^4)$		$\rho\,(N_e = 10^7)$	
$i - j$	*Present*	*Storey*	*Present*	*Storey*
1 – 2	4.06×10^4	5.85×10^4	6.69×10^2	7.49×10^2
1 – 5	2.24×10^4	2.27×10^4	2.19×10^3	2.62×10^3
1 – 8	2.89×10^4	2.83×10^4	1.15×10^4	1.26×10^4
2 – 3	8.79×10^3	1.26×10^4	2.14×10^2	2.17×10^2
2 – 5	5.89×10^3	5.83×10^3	–	–
2 – 6	6.87×10^3	6.93×10^3	7.70×10^2	9.23×10^2
2 – 8	8.65×10^3	8.47×10^3	3.45×10^3	3.78×10^3
2 – 9	–	–	3.54×10^3	3.82×10^3
2 – 13	3.84×10^3	4.07×10^3	5.15×10^3	5.39×10^3
3 – 4	1.49×10^3	1.94×10^3	3.20×10^1	3.26×10^1
3 – 6	3.83×10^3	3.91×10^3	–	–
3 – 9	–	–	2.56×10^3	2.74×10^3
3 – 15	–	–	2.02×10^3	2.38×10^3
4 – 15	–	–	1.04×10^3	1.24×10^3
8 – 12	3.90×10^3	3.82×10^3	–	–
8 – 14	–	–	5.36×10^2	7.49×10^2

the lowest 11 $3d^7$ fine-structure levels across nine temperatures of astrophysical importance.[1]

3.3 Line ratios

Combining the electron-impact excitation rates with the decay rates (*A*-values), it is possible to investigate important infrared and visible line ratios. For simplicity and purpose of this study, we neglect the recombination and ionization process from the neighbouring ion stages and focus on the populating mechanisms solely of Co III. Assuming local thermal equilibrium and detailed balance, we can derive the collisional radiative modelling approach detailed in (Griffin et al. 1997). We can therefore investigate selected transitions that have been suggested as temperature or density diagnostics.

We present in Table 5 a comparison of emissivities (ρ_{ij}) between our current results, and those from Storey & Sochi (2016) for particular transitions at electron densities $N_e = 10^4$ cm^{-3} and $N_e = 10^7$ cm^{-3}. The emissivities are calculated relative to the H β line [see equation (1) in Storey & Sochi (2016)], where the effective recombination coefficients $\bar{\alpha}_{4\to2}$ can be found in Hummer & Storey (1987) and Storey & Hummer (1995). The wavelengths are those from National Institute of Standards and Technology (NIST) and we use our current set of *A*-values. In general there is excellent agreement for all emissivities considered with the major outlier $\rho_{1\to2}$ found to be around 30 per cent at $N_e = 10^4$ cm^{-3}. This is evident from the strong $\Upsilon_{1\to2}$ from Fig. 5(a) at $T = 10^4$ K. By replacing this one effective collision strength to $\Upsilon_{1\to2}(T = 10\,000) = 4.18$, then the $\rho_{1\to2}$ differences are within a much more agreeable 8 per cent. A similar argument follows for the large differences in the $\rho_{2\to3}$ at low electron density.

Another useful quantity to investigate is the line ratio which is defined by

$$\mathcal{R} = \frac{I_{j\to i}}{I_{k\to m}} = \frac{N_j A_{j\to i}}{N_k A_{k\to m}} \frac{\lambda_{mk}}{\lambda_{ij}},$$

[1] The results are also in the form of an *adf04* file on http://open.adas.ac.uk and on QUB pure.

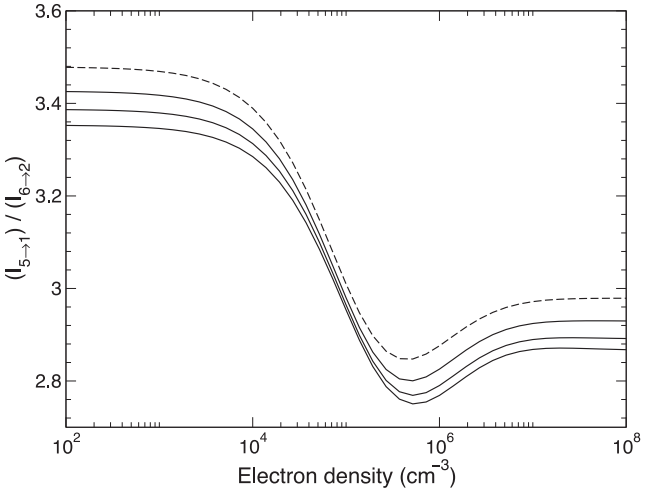

Figure 7. The line ratio [0.66 μm]/[0.69 μm] as a function of electron density (cm^{-3}). The dashed curve is the lowest temperature, $T = 3980$ K. The remaining solid black curves are for temperatures $T = 5010$, 6310, and 7940 K for decreasing line ratio.

where the populations of the *n*th level in terms of the ground state are given by N_n and the decay rates are the results from Section 2.1.

Fig. 7 depicts the results of the line ratio [0.66 μm]/[0.69 μm] which corresponds to the transitions,

$$\frac{I_{5\to1}}{I_{6\to2}} = \frac{3d^7\ a^4P_{5/2} \to 3d^7\ a^4F_{9/2}}{3d^7\ a^4P_{3/2} \to 3d^7\ a^4F_{7/2}},$$

as a function of electron density for particular temperatures. The dashed line provides the lowest temperature, $T = 3980$ K, with increasing T to $T = 5010$, 6310 and 7940 K. The line ratio is constant for densities $N_e < 10^4$ cm^{-3} and also $N_e > 10^7$ cm^{-3} for the temperatures considered. This could be considered a useful diagnostic for densities in the range of 10^4 cm^{-3} $< N_e < 3 \times 10^5$ cm^{-3} where it remains constant for increasing temperatures before it reaches its minimum $\approx 5 \times 10^5$ cm^{-3}

Next we consider lines suggested by Ruiz-Lapuente (1995), (around the wavelength region 6000–6500 Å) to be applied as density diagnostics. At 10 000 K, we can see the photon emissivity coefficients of the $8 \to 1$ and $8 \to 2$ lines becomes more dominant for increasing temperatures, and are in the ideal wavelength region. Telesco et al. (2015) also suggests the $2 \to 1$, 11.88 μm as a useful diagnostic line. We finally present the results of three line ratios,

$$\frac{I_{2\to1}[11.88\ \mu m]}{I_{5\to1}[0.66\ \mu m]} = \frac{3d^7\ a^4F_{7/2} \to 3d^7\ a^4F_{9/2}}{3d^7\ a^4P_{5/2} \to 3d^7\ a^4F_{9/2}},$$

$$\frac{I_{2\to1}[11.88\ \mu m]}{I_{8\to1}[0.59\ \mu m]} = \frac{3d^7\ a^4F_{7/2} \to 3d^7\ a^4F_{9/2}}{3d^7\ a^2G_{9/2} \to 3d^7\ a^4F_{9/2}},$$

and,

$$\frac{I_{2\to1}[11.88\ \mu m]}{I_{8\to2}[0.62\ \mu m]} = \frac{3d^7\ a^4F_{7/2} \to 3d^7\ a^4F_{9/2}}{3d^7\ a^2G_{9/2} \to 3d^7\ a^4F_{7/2}}.$$

We plot all three line ratios above in Fig. 8 as a function of electron temperature. The red dashed curve is the lowest electron density in each subfigure, $N_e = 10^2$ cm^{-3}, and the remaining solid curves correspond to $N_e = 10^4$, 10^5, and 10^6 cm^{-3}. Each line ratio is a varying function of increasing temperature across the range of interest. The line ratios for the two lowest densities are generally unchanged, and therefore they provide useful diagnostics for this

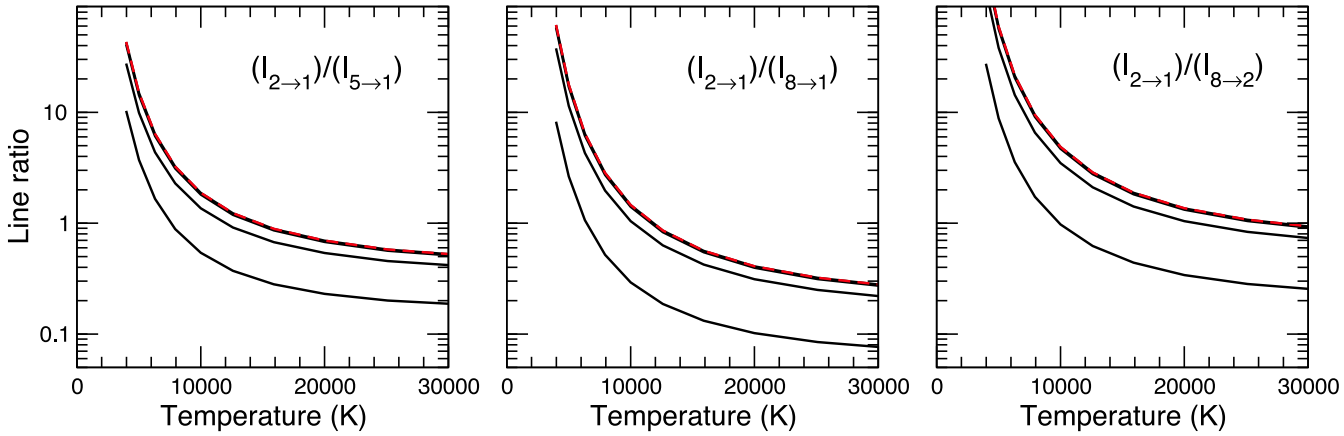

Figure 8. The line ratio [11.88 μm]/[0.66 μm] (left), [11.88 μm]/[0.59 μm] (middle), and [11.88 μm]/[0.62 μm] (right) as a function of electron temperature (K). The red, dashed curve is the lowest density, $N_e = 10^2$ cm^{-3}. The remaining solid black curves are for densities $N_e = 10^4$ cm^{-3}, 10^5, and 10^6 cm^{-3} for decreasing line ratio.

density range. As $N_e = 10^5$ cm^{-3} and beyond, the line ratio begins to diverge, and becomes constant again for even larger densities.

4 CONCLUSION

In this paper, we present an extensive set of atomic data for the photoionization of Co II and the electron-impact excitation of Co III. Initially we have exploited the computer code GRASP0 to obtain a description of the atomic wavefunctions and generate energy levels for the 292 fine-structure bound target states and the corresponding *A*-values for transitions between these levels. Furthermore, the DARC computer package has been employed to extend the problem to include photon and electron interactions. We present statistically weighted, level-resolved ground and metastable photoionization cross-sections for the Co II ion as well as collision strengths and Maxwellian averaged effective collision strengths describing the electron-impact excitation of the Co III ion. Comparisons are made with other works where possible and good agreement is found where a comparison is available. The reliability of the atomic data presented has been rigorously tested through a variety of means, such as the sophistication of the current calculations where great care has been taken to ensure the inclusion of important correlation and configuration-interaction in the wavefunction expansions. In addition the complex resonance structures in the cross-sections (photoionization and excitation) have been accurately resolved through a series of calculations incorporating mesh sizes with finer and finer energy increments. A proper consideration was also taken of the contributions from the high partial waves to ensure convergence of the collision strengths for the allowed transitions in particular (which are not presented in this work). A conclusive assessment of the accuracy of the presented Maxwellian averaged collision strengths will necessarily come from any subsequent astrophysical or diagnostic application. In Section 3.3 the electron-impact excitation rates were combined with the decay rates (*A*-values) to investigate important infrared and visible line ratios. During this process we were able to identify useful transitions that could be used as temperature and/or density sensitive diagnostic lines.

ACKNOWLEDGEMENTS

The work conducted has been supported by STFC through the grant ST/K000802/1. The authors would also like to acknowledge time on the Stuttgart, Hazelhen machine under the PAMOP (44009) project where all calculations have been performed.

REFERENCES

Aggarwal K. M., Bogdanovich P., Karpuškienė R., Keenan F. P., Kisielius R., Stancalie V., 2016, At. Data Nucl. Data Tables, 107, 140
Badnell N. R., 1986, J. Phys. B: At. Mol. Phys., 19, 3827
Bautista M. A., Fivet V., Ballance C., Quinet P., Ferland G., Mendoza C., Kallman T. R., 2015, ApJ, 808, 174
Bergemann M., Pickering J. C., Gehren T., 2010, MNRAS, 401, 1334
Burgess A., 1974, J. Phys. B: At. Mol. Phys., 7, L364
Burgess A., Tully J. A., 1992, A&A, 254, 436
Burke P. G., 2011, R-Matrix Theory of Atomic Collisions. Springer-Verlag, Berlin
Burke P. G., Taylor K. T., 1975, J. Phys. B: At. Mol. Phys., 8, 2620
Burke P. G., Hibbert A., Robb W. D., 1971, J. Phys. B: At. Mol. Phys., 4, 153
Cardon B. L., Smith P. L., Scalo J. M., Testerman L., Whaling W., 1982, ApJ, 260, 395
Cowan R. D., 1981, The Theory of Atomic Structure and Spectra. Univ. California Press, Berkeley
Cunto W., Mendoza C., 1992, Rev. Mex. Astron. Astrophys., 23, 107
Cunto W., Mendoza C., Ochsenbein F., Zeippen C. J., 1993, A&A, 275, L5
Dessart L., Hillier D. J., Blondin S., Khokhlov A., 2014, MNRAS, 441, 3249
Diamond T. R., Hoeflich P., Gerardy C. L., 2015, ApJ, 806, 107
Dworetsky M. M., 1982, Observatory, 102, 138
Dworetsky M. M., Trueman M. R. G., Stickland D. J., 1980, A&A, 85, 138
Eissner W., Jones M., Nussbaumer H., 1974, Comput. Phys. Commun., 8, 270
Federman S. R., Sheffer Y., Lambert D. L., Gilliland R. L., 1993, ApJ, 413, L51
Fernández-Menchero L., Del Zanna G., Badnell N. R., 2015, MNRAS, 450, 4174
Fivet V., Quinet P., Bautista M. A., 2016, A&A, 585, A121
Fontes C. J. et al., 2015, J. Phys. B: At. Mol. Phys., 48, 144014
Gerardy C. L. et al., 2007, ApJ, 661, 995
Gharaibeh M. F. et al., 2011, J. Phys. B: At. Mol. Phys., 44, 175208
Griffin D. C., Pindzola M. S., Shaw J. A., Badnell N. R., O'Mullane M., Summers H. P., 1997, J. Phys. B: At. Mol. Phys., 30, 3543
Griffin D. C., Badnell N. R., Pindzola M. S., 1998, J. Phys. B: At. Mol. Phys., 31, 3713
Hansen J. E., Raassen A. J. J., Uylings P. H. M., 1984, ApJ, 277, 435
Hillier D. J., 2011, Ap&SS, 336, 87

Hummer D. G., Storey P. J., 1987, MNRAS, 224, 801
Kromer M., Sim S. A., 2009, MNRAS, 398, 1809
Li H., McCray R., Sunyaev R. A., 1993, ApJ, 419, 824
Lucy L. B., 2005, A&A, 429, 19
Mazzali P. A., Chugai N., Turatto M., Lucy L. B., Danziger I. J., Cappellaro E., della Valle M., Benetti S., 1997, MNRAS, 284, 151
Meikle W. P. S., Spyromilio J., Varani G. F., Allen D. A., 1989, MNRAS, 238, 193
Müller A. et al., 2009, J. Phys. B: At. Mol. Phys., 42, 235602
Nussbaumer H., Storey P. J., 1988, A&A, 200, L25
Pickering J. C., Raassen A. J. J., Uylings P. H. M., Johansson S., 1998, ApJS, 117, 261
Quinet P., 1998, A&AS, 129, 147
Ramsbottom C. A., 2009, At. Data Nucl. Data Tables, 95, 910
Ramsbottom C. A., Hudson C. E., Norrington P. H., Scott M. P., 2007, A&A, 475, 765
Reilman R. F., Manson S. T., 1979, ApJS, 40, 815
Ruiz-Lapuente P., 1995, in Adelman S. J., Wiese W. L. eds, ASP Conf. Ser. Vol. 78, Calculated Late-time Spectra of Type IA Supernovae: Atomic Needs and Astrophysical Interest. Astron. Soc. Pac., San Francisco, p. 291
Scott N. S., Burke P. G., 1980, J. Phys. B: At. Mol. Phys., 13, 4299
Sim S. A., 2007, MNRAS, 375, 154
Smith K. C., Dworetsky M. M., 1993, A&A, 274, 335
Snow T. P., Jr, Weiler E. J., Oegerle W. R., 1979, ApJ, 234, 506
Storey P. J., Hummer D. G., 1995, MNRAS, 272, 41
Storey P. J., Sochi T., 2016, MNRAS, 459, 2558
Storey P. J., Zeippen C. J., Sochi T., 2016, MNRAS, 456, 1974
Sugar J., Corliss C., 1985, Atomic Energy Levels of the Iron-Period Elements: Potassium Through Nickel. American Chemical Society, Washington
Telesco C. M. et al., 2015, ApJ, 798, 93
Thackeray A. D., 1976, MNRAS, 174, 59
Tyndall N. B., Ramsbottom C. A., Ballance C. P., Hibbert A., 2016, MNRAS, 456, 366
Verner D. A., Yakovlev D. G., Band I. M., Trzhaskovskaya M. B., 1993, At. Data Nucl. Data Tables, 55, 233
Zatsarinny O., Bartschat K., 2004, J. Phys. B: At. Mol. Phys., 37, 4693
Zatsarinny O., Froese Fischer C., 2000, J. Phys. B: At. Mol. Phys., 33, 313
Zethson T., Gull T. R., Hartman H., Johansson S., Davidson K., Ishibashi K., 2001, AJ, 122, 322

This paper has been typeset from a TEX/LATEX file prepared by the author.